



Modeling and predicting cancer clonal evolution with reinforcement learning

Stefan Ivanovic and Mohammed El-Kebir

Genome Res. 2023 33: 1078-1088 originally published online June 21, 2023

Access the most recent version at doi:[10.1101/gr.277672.123](https://doi.org/10.1101/gr.277672.123)

References This article cites 31 articles, 3 of which can be accessed free at:
<http://genome.cshlp.org/content/33/7/1078.full.html#ref-list-1>

Creative Commons License This article is distributed exclusively by Cold Spring Harbor Laboratory Press for the first six months after the full-issue publication date (see <https://genome.cshlp.org/site/misc/terms.xhtml>). After six months, it is available under a Creative Commons License (Attribution-NonCommercial 4.0 International), as described at <http://creativecommons.org/licenses/by-nc/4.0/>.

Email Alerting Service Receive free email alerts when new articles cite this article - sign up in the box at the top right corner of the article or [click here](#).



To subscribe to *Genome Research* go to:
<https://genome.cshlp.org/subscriptions>

Method

Modeling and predicting cancer clonal evolution with reinforcement learning

Stefan Ivanovic¹ and Mohammed El-Kebir^{1,2}

¹Department of Computer Science, University of Illinois at Urbana-Champaign, Urbana, Illinois 61801, USA; ²Cancer Center at Illinois, University of Illinois Urbana-Champaign, Urbana, Illinois 61801, USA

Cancer results from an evolutionary process that typically yields multiple clones with varying sets of mutations within the same tumor. Accurately modeling this process is key to understanding and predicting cancer evolution. Here, we introduce clone to mutation (CloMu), a flexible and low-parameter tree generative model of cancer evolution. CloMu uses a two-layer neural network trained via reinforcement learning to determine the probability of new mutations based on the existing mutations on a clone. CloMu supports several prediction tasks, including the determination of evolutionary trajectories, tree selection, causality and interchangeability between mutations, and mutation fitness. Importantly, previous methods support only some of these tasks, and many suffer from overfitting on data sets with a large number of mutations. Using simulations, we show that CloMu either matches or outperforms current methods on a wide variety of prediction tasks. In particular, for simulated data with interchangeable mutations, current methods are unable to uncover causal relationships as effectively as CloMu. On breast cancer and leukemia cohorts, we show that CloMu determines similarities and causal relationships between mutations as well as the fitness of mutations. We validate CloMu's inferred mutation fitness values for the leukemia cohort by comparing them to clonal proportion data not used during training, showing high concordance. In summary, CloMu's low-parameter model facilitates a wide range of prediction tasks regarding cancer evolution on increasingly available cohort-level data sets.

[Supplemental material is available for this article.]

Cancer results from an evolutionary process during which somatic mutations accumulate in a population of cells. This process results in a tumor composed of multiple subpopulations of cells, or *clones*, with varying sets of mutations (Nowell 1976). As different clones within the same tumor harbor different sets of mutations, they have varying phenotypes and fitness (Yates and Campbell 2012). Moreover, although each cancer results from a separate evolutionary process, there are repeated patterns of evolution that recur across cancers (Hanahan and Weinberg 2000). The key challenge in comparative cancer phylogenetics revolves around identifying such repeated evolutionary patterns or trajectories (Turajlic et al. 2018). This is a challenging problem and requires a mathematical model that accurately captures the somatic evolutionary process of cancers.

There are many existing methods for modeling cancer evolution with single-nucleotide variations (SNVs), which can be distinguished into three classes. The first class of methods is based on tree generative models, which include TreeMHN (Luo et al. 2023) and HINTRA (Khakabimamaghani et al. 2019). A generative model restricted to paths and trained using inverse reinforcement learning was considered by Kalantari et al. (2020). The second class of methods is consensus tree models, which seek a small number of consensus trees that summarize common patterns among patient trees. Methods such as REVOLVER (Caravagna et al. 2018), RECAP (Christensen et al. 2020), CONETT (Hodzic et al. 2020), and MASTRO (Pellegrina and Vandin 2022) fall into this category. The third class of methods uses statistical tests to evaluate patterns of co-occurrence and mutual exclusivity of mutations across trees without trying to fully model the evolutionary process. GeneAccord is one such method (Kuipers et al. 2021). Although

consensus tree methods have the advantage of being able to detect complicated patterns in tumor evolution, tree generative models must be carefully designed to accommodate complex multimutation effects. An example of such an effect is when mutations s and t only increase the probability of mutation r when they are present together. Conversely, tree generative methods have the advantage of being able to directly model how a clone's mutations affect the probability of new mutations occurring.

A second distinguishing feature of current methods is how the number of model parameters scales with an increasing number m of mutations. Having the number of parameters scale too rapidly with the number of mutations can lead to greatly overfitting on real data sets, as well as a prohibitive running time. One such example is HINTRA (Khakabimamaghani et al. 2019), in which the number of parameters grows exponentially in m , and consequently, it can only accommodate a handful of mutations. On the other hand, models that directly measure relationships between pairs of mutations or fit trees with edges determined by pairs of mutations have their parameters grow quadratically in the number of mutations, reducing overfitting and running time (Caravagna et al. 2018; Christensen et al. 2020; Hodzic et al. 2020; Kuipers et al. 2021; Luo et al. 2023).

Finally, current methods can be distinguished by the prediction tasks they support. The majority of current methods, spanning both tree generative (Khakabimamaghani et al. 2019; Luo et al. 2023) and consensus tree methods (Caravagna et al. 2018; Christensen et al. 2020; Hodzic et al. 2020), aim to identify evolutionary trajectories, which correspond to ordered sequences or

Corresponding author: melkebir@illinois.edu

Article published online before print. Article, supplemental material, and publication date are at <https://www.genome.org/cgi/doi/10.1101/gr.277672.123>.

© 2023 Ivanovic and El-Kebir This article is distributed exclusively by Cold Spring Harbor Laboratory Press for the first six months after the full-issue publication date (see <https://genome.cshlp.org/site/misc/terms.xhtml>). After six months, it is available under a Creative Commons License (Attribution-NonCommercial 4.0 International), as described at <http://creativecommons.org/licenses/by-nc/4.0/>.

trees of mutations reflecting repeated patterns of evolution. Additionally, several methods use signals from across patients to resolve uncertainty in phylogeny inference within a single patient (Caravagna et al. 2018; Khakabimamaghani et al. 2019; Christensen et al. 2020; Hodzic et al. 2020). Another task is the prediction of causality between pairs of mutations. This can be performed in a signed manner, distinguishing between causal and inhibitory relationships, as well as in a bidirectional manner, distinguishing between a mutation s causing t and vice versa. Although TreeMHN (Luo et al. 2023) supports both signed and bidirectional causal relationships, GeneAccord (Kuipers et al. 2021) only supports signed causal relationships. On the other hand, consensus tree methods are unable to support inhibitory causal relationships (Caravagna et al. 2018; Christensen et al. 2020; Hodzic et al. 2020).

In this work, we identify three additional tasks that no current evolutionary trajectory method supports. First is determining the fitness of a mutation, namely, assessing how having that mutation impacts the rate at which a clone develops. Second, although previous work has focused on identifying co-occurrence and mutual exclusivity of mutations at the patient level without directly considering downstream mutation evolution (Leiserson et al. 2015; Dao et al. 2017; Kim et al. 2017; Kuipers et al. 2021), we introduce the task of determining sets of interchangeable mutations that have similar impacts on subsequent mutation evolution. Third is determining collections of evolutionary trajectories between sets of interchangeable mutations. To accommodate these new and all previous tasks, we introduce clone to mutation (CloMu). Underlying CloMu is a tree generative model, which uses a low-parameter neural network trained using reinforcement learning, resulting in fewer parameters than all current models while maintaining high flexibility to model complex multimutation effects. In summary, this study aims to introduce a method for accurately performing a wide variety of prediction tasks on cohort-level cancer phylogeny data.

Results

Overview of CloMu

We take as input tumor phylogenies of n patients with m total mutations. Because of uncertainty in tree inference from sequencing

data (Qi et al. 2019), each patient p has a set \mathcal{T}_p of multiple possible trees $\{T_1, \dots, T_{|\mathcal{T}_p|}\}$. Similarly to HINTRA (Khakabimamaghani et al. 2019) and TreeMHN (Luo et al. 2023), we make the *independent clonal evolution* assumption that the event of a clone acquiring a new mutation only depends on the genotype of that clone. Each clone can be represented as a binary vector $\mathbf{c} \in \{0, 1\}^m$, where $c_s = 1$ if the clone harbors mutation s and $c_s = 0$ otherwise. The goal is to identify a model that best describes the causal relationship between clones \mathbf{c} and acquired mutations $[m] = \{1, \dots, m\}$ under our assumption for the observed data $\mathcal{T}_1, \dots, \mathcal{T}_n$. We model this using the function $f_\theta: \{0, 1\}^m \times [m] \rightarrow \mathbb{R}$ such that $f_\theta(\mathbf{c}, s)$ is the logarithm of the rate at which mutation s occurs on clone \mathbf{c} (Fig. 1A). Starting with an initial tree $T^{(0)}$ with just a single node corresponding to the normal clone $\mathbf{c}_0 = [0, \dots, 0]^T$, we sample the mutation that occurs next, yielding a new tree $T^{(1)}$ with an additional clone \mathbf{c}_1 that introduces one mutation w.r.t. \mathbf{c}_0 . Repeating this process yields a new partial tree $T^{(k)}$ after each mutation is introduced, as shown in Supplemental Figure S1. Note that any tree can be generated through this process.

Our goal is to find the model parameters θ^* that maximize the probability of observing the input data, namely, $\theta^* = \operatorname{argmax}_\theta \Pr(\mathcal{T}_1, \dots, \mathcal{T}_n | f_\theta)$. To do so, we must estimate the probability of any input tree T denoted by $\Pr(T | f_\theta)$, noting the fact that there are multiple ways of generating each tree (Fig. 1B). This leads to the following problem, which we describe in more detail in the Methods.

Problem 1 (INDEPENDENT CLONAL EVOLUTION). Given a cohort of tumor phylogenies $\mathcal{T}_1, \dots, \mathcal{T}_n$ for n tumors on m mutations, find model parameters θ such that $\Pr(\mathcal{T}_1, \dots, \mathcal{T}_n | f_\theta)$ is maximized.

To solve the INDEPENDENT CLONAL EVOLUTION problem, we introduce CloMu, which represents the model f_θ using a two-layer neural network with a small number $L=5$ of hidden neurons for the function f_θ (Fig. 1C). This neural network is trained via reinforcement learning (Methods).

Although we train the model f_θ only once for each data set $\{\mathcal{T}_1, \dots, \mathcal{T}_n\}$ by solving a single instance of the INDEPENDENT CLONAL EVOLUTION problem, its outputs can be postprocessed to complete a wide variety of tasks, gaining insights into cancer

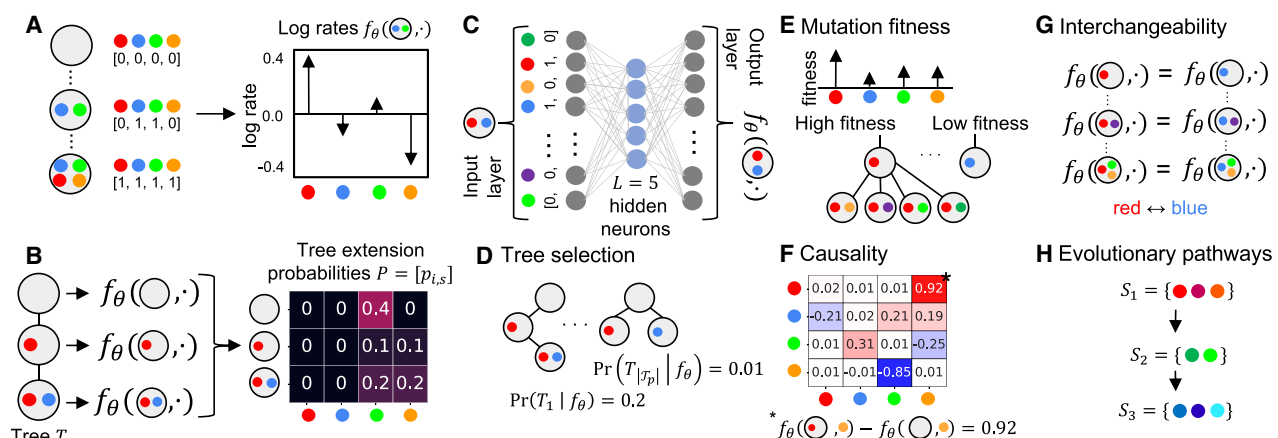


Figure 1. Overview of CloMu. (A) Using the independent clonal evolution assumption, our model determines a log rate $f_\theta(\mathbf{c}, s)$ of any clone $\mathbf{c} \in \{0, 1\}^m$ acquiring a mutation $s \in [m]$. (B) This in turn enables us to compute probabilities $P = [p_{i,s}]$ that the next mutation to occur on a tree T is mutation s at node/clone \mathbf{c} . The resulting INDEPENDENT CLONAL EVOLUTION problem seeks model parameters θ that maximize the data probability $\Pr(\mathcal{T}_1, \dots, \mathcal{T}_n | f_\theta)$ of a cohort of trees for n patients. (C) CloMu represents f_θ using a low-parameter, two-layer neural network that is trained via reinforcement learning. We use the model for five prediction tasks: (D) tree selection for each patient, (E) determination of mutation fitness, (F) causality inference for pairs of mutations, (G) identification of interchangeable mutations, and (H) identification of their evolutionary pathways.

evolution. The exact mathematical details of these tasks are discussed in the Methods, but we give a brief summary here. First, one can use the model to reduce uncertainty in tree inference by determining which phylogenies are most likely to be the true phylogeny for a particular patient (Fig. 1D). Second, the model can be used to determine the fitness of different mutations based on how they affect the likelihood of new mutations occurring on a clone (Fig. 1E). Third, the model can be used to infer co-occurrence patterns between pairs of mutations, which we refer to as causal relationships (Fig. 1F). Fourth, the model can be used to detect interchangeable mutations, namely, mutations with similar downstream mutation effects that are mutually exclusive or co-occurring, by assessing the values of the L hidden neurons when a clone is taken as an input (Fig. 1G). Fifth, we can determine pathways of interchangeable mutations (Fig. 1H).

Benchmarking on simulated data

We use simulations with known ground truth to assess the performance of CloMu and several existing methods on the prediction tasks (outlined in the section “Prediction tasks”). We consider four sets of simulation instances: (1) simulations to assess tree selection and causality, (2) simulations to assess mutation interchangeability and evolutionary pathways, as well as previous simulations generated in the (3) RECAP (Christensen et al. 2020) and (4) TreeMHN (Luo et al. 2023) papers (Table 1). We include TreeMHN (Luo et al. 2023), RECAP (Christensen et al. 2020), REVOLVER (Caravagna et al. 2018), and GeneAccord (Kuipers et al. 2021) in the benchmarking, and refer to Supplemental Material B.2 for parameter settings.

We begin by discussing the generation of the first set of simulation instances to assess tree selection, causality, and mutation interchangeability. We focus on the simplest case with no interchangeable mutations. We considered $m = 10$ mutations, subdivided into five driver mutations and five passenger mutations. For every ordered pair (s, t) of distinct driver mutations, there is a 50% chance that s causes t . Let X be the resulting set of causal relationship pairs. Note that $|X| \leq 20$ as there are 20 ordered pairs (s, t) of distinct driver mutations. For each pair $(s, t) \in [m] \times [m]$ of mutations, we set the rate multiplier to $g(s, t) = 11$ if $(s, t) \in X$ and to $g(s, t) = 1$ otherwise. We defined the rate $\lambda(\mathbf{c}, t)$ of a clone $\mathbf{c} \in \{0, 1\}^m$ acquiring a mutation t as $\prod_{s=1, c_s=1}^m g(s, t)$. We define the log rate $f(\mathbf{c}, t)$ of a clone $\mathbf{c} \in \{0, 1\}^m$ acquiring a mutation t as $\log(\lambda(\mathbf{c}, t))$. Given a number $n = 500$ of patients, we generated one ground-truth tree T_p^* for each patient $p \in [n]$ by first drawing the number ℓ of mutations of the tree T_p^* uniformly from $\{5, 6, 7\}$. We used the rates $\lambda(\mathbf{c}, t)$ to construct T_p^* following the genera-

tive process with ℓ mutations discussed in the section “Overview of CloMu”—with $f_\theta(\mathbf{c}, t)$ replaced with $f(\mathbf{c}, t)$ [or, equivalently, $\exp(f_\theta(\mathbf{c}, t))$ replaced with $\lambda(\mathbf{c}, t)$]. Although not required by CloMu, we imposed the infinite sites assumption in our simulations. Finally, we simulated five bulk DNA sequencing samples and performed clonal tree enumeration, resulting in sets T_1, \dots, T_n of trees per patient with a varying number of trees per patient as shown in Supplemental Figure S3. We generated a total of 20 simulation instances, denoted simulations I-a. Additionally, to assess the effect of interchangeable mutations, we generated two additional sets of 20 simulation instances, denoted simulations I-b and I-c, with, respectively, five pairwise disjoint sets of two and three interchangeable mutations among $m = 10$ and $m = 15$ total mutations. Finally, we generated a set of 20 simulation instances, denoted simulation II, to assess evolutionary pathway identification. Note that each simulation instance is generated independently and thus does not necessarily share randomly generated properties such as causal relationships with other instances. For further details, see Table 1 and Supplemental Material B.1.

For the tree selection task, we compared CloMu to RECAP and REVOLVER on simulations I-a (Table 1). For each simulation instance, we determined the tree selection accuracy defined as the fraction of patients for which each method correctly identified the ground-truth tree. Figure 2A shows that CloMu achieves the highest tree selection accuracy (median, 0.76), followed by REVOLVER (median, 0.70) and then RECAP (median, 0.65). To assess causality inference, we compared CloMu (using absolute causality) against TreeMHN and GeneAccord, which directly support causality inference (Table 2). Although RECAP and REVOLVER do not directly support this task, we used a simple heuristic based on the frequency of mutation pairs/edges (s, t) among selected trees (Supplemental Material B.2). Figure 2B shows that CloMu and TreeMHN performed near perfectly on this task (median recall and precision of 1.0), followed by RECAP and REVOLVER (respectively, median recall, 0.76 and 0.77; median precision, 1.0 and 1.0) and then GeneAccord (median recall and precision, 0.78 and 0.85). Additionally, we used bootstrapping to assess the confidence intervals on absolute causality predictions, showing that the lower bound for pairs of mutations with a true causal relationship vastly exceeds the upper bound for pairs of mutations without a true causal relationship (Supplemental Material B.3.1; Supplemental Figs. S4, S5). Moreover, we assessed the effect of decreasing numbers of patients and mutations per patient as well as an increased number of passenger mutations and varying causation effect sizes, showing good performance of CloMu in each simulation condition (Supplemental Materials B.3.2–B.3.5; Supplemental Figs. S6–S10).

Table 1. Characteristics of simulation data sets

	No. of Drivers	No. of mutations	No. of interchangeable mutation sets	No. of interchangeable mutations per set	No. of patients	Signed causality	No. of paths	No. of instances.
(I-a)	5	10	NA	NA	500	No	NA	20
(I-b)	10	10	5	2	400	Yes	NA	20
(I-c)	15	15	5	3	600	Yes	NA	20
(II)	{3, ..., 18}	20	No. of paths. $\times 3$	{1, 2, 3}	500	No	{1, 2}	30
(III)	NA	{5, 12}	NA	NA	{50, 100}	NA	NA	400
(IV)	{10, 15, 20}	{10, 15, 20}	NA	NA	300	Yes	NA	60

We considered six sets of simulations, labeled I-a to IV with varying number of driver mutations, total number of mutations, number of interchangeable mutation sets, number of interchangeable mutations per set, number of patients, the presence of both causation and inhibition, the number of evolutionary pathways of interchangeable mutations and the total number of instances. Simulations III correspond to previously published RECAP simulations (Christensen et al. 2020). Simulations IV correspond to previously published TreeMHN simulations (Luo et al. 2023).

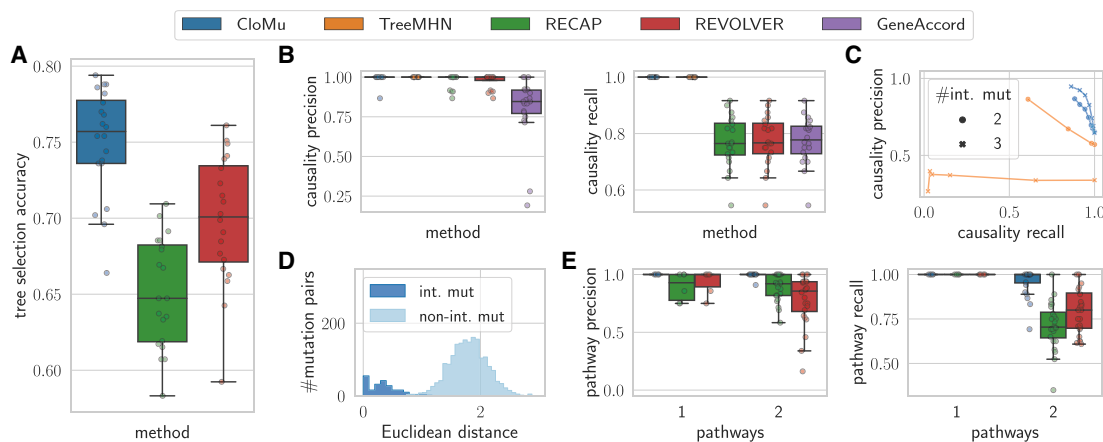


Figure 2. CloMu outperforms existing methods on several prediction tasks on simulated data with known ground truth. (A) Tree selection accuracy measures the ability to correctly identify the ground-truth tree from a set T_p of possible trees generated from simulated bulk sequencing for each patient p . (B) Causality precision and recall measure the ability to determine positive causal relationships between ordered pairs of mutations. Panels A and B show results for simulations I-a. (C) On simulations I-b and I-c, causality precision and recall measure the ability to identify causation and inhibition between pairs of mutations in the presence of mutation interchangeability. (D) On simulations II, interchangeability detection shows that the latent representations generated by our model are meaningful, accurately encapsulating mutation similarity. (E) On simulations II, pathway precision and recall measure the ability to determine evolutionary pathways in the presence of both interchangeability and complex multimutation interactions.

Upon observing CloMu and TreeMHN's near perfect performance, we decided to include interchangeable mutations as well as inhibitory relationships (simulations I-b and I-c) (see Table 1). We refer to [Supplemental Material B.2](#) and [Supplemental Table S2](#) for the updated definitions of causality precision and recall for the case of signed causality, which match TreeMHN's definitions. We found that CloMu maintained good performance whereas TreeMHN's performance dropped, especially with increasing numbers of interchangeable mutations (Fig. 2C). This was also the case when all causal relationships between interchangeable mutations were made inhibitory ([Supplemental Material B.3.8](#); [Supplemental Fig. S14](#)). We believe the reason TreeMHN performed poorly on these instances is its assumption of independent causal relationships between pairs of mutations. The number $m^2 - m$ of causal relationships that TreeMHN must independently determine grows quadratically with the number m of mutations. In contrast, if CloMu's neural network learns that there are only $k \ll m$ noninterchangeable types of mutations, it must only detect k^2 causal relationships. Specifically, for these simulation instances, there were $k = 5$ sets of interchangeable mutations among a total of $m \in \{10, 15\}$ mutations (see [Supplemental Material B.1](#)), leading to $k^2 = 25$ causal relationships for CloMu to detect and $m^2 - m \in \{90, 210\}$ for TreeMHN. One potential concern is that the high performance of CloMu and avoidance of overfitting is only owing to the small number of parameters caused by our choice of $L = 5$ hidden neurons. However, in [Supplemental Material B.3.9](#), we show that with an increased number $L = 20$ of hidden neurons, CloMu even gives slightly more accurate causal relationship predictions ([Supplemental Fig. S15](#)). [Supplemental Material B.3.10](#) and [Supplemental Figures S17](#) and [S18](#) show CloMu's accuracy on simulations in which mutations have related effects rather than being exactly interchangeable. The effects of mutations are not independent despite not being identical, as shown in [Supplemental Figure S16](#). We show CloMu's ability to accurately identify multimutation causality effects in [Supplemental Material B.3.11](#) and [Supplemental Figure S19](#).

We now focus on simulations II to further assess performance on determining interchangeable mutations and their evolutionary

pathways. [Figure 2D](#) shows that CloMu accurately distinguishes between pairs of interchangeable and noninterchangeable mutations as assessed by the Euclidean distance on CloMu's latent representation. We note that these simulations contain causal effects that only occur in the presence of specific combinations of mutations on a clone ([Supplemental Material B.1](#)). Accurately determining the pathways requires modeling these multimutation effects, as shown in [Supplemental Figure S2](#). To have some baseline for comparison, we applied a heuristic to determine the pathways of interchangeable mutations from the trees selected by RECAP and REVOLVER ([Supplemental Material B.2](#)). Briefly, our heuristic measured the number of times each edge occurs in selected trees for this method and then inferred the pathway edges as all edges that occur above some frequency. TreeMHN and GeneAccord could not be adapted to form a baseline because they do not select trees. Additionally, they have no way of modeling effects that only occur in the presence of a combination of mutations. We determined the number of true and false positives, as well as false negatives, by comparing the set of true pathway edges and predicted edges, enabling us to compute pathway precision and recall. We found that CloMu, RECAP, and REVOLVER all achieved a median pathway recall of 1.0 in simulations with only one pathway ([Fig. 2E](#)). However, CloMu outperformed the baselines in terms of precision (overall median, 1.0 vs. 0.92 and 0.87 for RECAP and REVOLVER, respectively), and especially for cases with two evolutionary pathways, it additionally outperformed the baseline methods in terms of recall (overall median, 1.0 vs. 0.75 and 0.83 for RECAP and REVOLVER, respectively).

Finally, we ran CloMu on data generated in the RECAP and TreeMHN papers, denoted as simulations III and IV, respectively ([Table 1](#)). We found that we matched RECAP's performance ([Supplemental Material B.3.12](#); [Supplemental Fig. S20](#)) but that CloMu was outperformed by TreeMHN when using $L = 5$ hidden neurons but achieved approximately similar performance when using a linear model with no hidden neurons ([Supplemental Material B.3.13](#); [Supplemental Fig. S21](#)). It is important to note that this results from the absence of interchangeable mutations or any mutations with shared causal properties in TreeMHN's

Table 2. Overview of methods for detecting patterns of cancer evolution

Method	Tree model	No. of parameters	Evolutionary trajectories	Tree selection	Multimutation effects	Signed causality	Bidirectional causality	Mutation fitness	Interchangeable mutations
CloMu	Generative	$O(mL)$	✓	✓	✓	✓	✓	✓	✓
TreeMHN	Generative	$O(m^2)$	✓	✓/X ^b	X	✓	✓	✓/X ^b	X
HINTRA	Generative	$O(m2^m)$	✓	✓	✓	X	✓	X	X
RECAP	Consensus	$O(m^2)$	✓	✓	✓	X	✓	X	X
CONETT	Consensus	$O(m^2)$	✓	✓	✓	X	✓	X	X
REVOLVER	Consensus	$O(m^2)$	✓	✓	✓	X	✓	X	X
GeneAccord	Statistical test ^a	$O(m^2)$	X	X	X	✓	X	X	X

For each method, we specify, from left to right, the underlying tree model, the number of parameters, support for evolutionary trajectories, tree selection, multimutation effects, signed and bidirectional causality inference, mutation fitness, and interchangeable mutations and their pathways.

^aGeneAccord does not contain a generative model of trees nor does it seek to infer a tree. Rather it takes as input a set of trees and assesses the causality between all pairs of mutations using a statistical test.

^bAlthough the feature is unimplemented, it could be supported by TreeMHN's model.

simulations. Such mutations are present in real data as we will show. As previously stated, our model uses the independent clonal evolution assumption. To show that our model is robust to violations in this assumption, we generated causal relationship simulations with clonal cooperation, showing robustness by maintaining high causal inference performance on these data (Supplemental Material B.3.6; Supplemental Fig. S11). To test robustness to the inclusion of highly incorrect trees, we additionally generated simulations in Supplemental Material B.3.7, achieving highly accurate causal relationship prediction (Supplemental Fig. S12) and tree selection (Supplemental Fig. S13). Naturally, the quality of CloMu's outputs is limited by the quality of the patterns that exist in the input trees. In Supplemental Material B.3.7, we also show that CloMu does not predict causal relationships when all input trees are randomly generated.

In summary, this simulation study shows that CloMu is a versatile model and supports a wide variety of prediction tasks. CloMu's low-parameter neural network affords it the flexibility to model complex multimutation interactions while retaining resistance to overfitting.

CloMu identifies high-fitness mutations and causal relationships in a breast cancer cohort

We applied CloMu to a breast cancer cohort composed of 1918 tumors from 1756 patients that were sequenced using a gene panel (Razavi et al. 2018). We used the same processing steps as in the RECAP paper (Christensen et al. 2020), restricting our analysis to SNVs that occur in copy-neutral autosomal regions followed by running SPRUCE (El-Kebir et al. 2016) to obtain a set T_p for each patient p . As in the RECAP analysis, we only retained mutations that occurred in at least 100 patients and removed patients that did not contain any of these recurrent mutations. CloMu can be run on arbitrarily large trees; however, patients with vast numbers (hundreds or thousands) of possible trees can greatly increase the computational requirements of running CloMu if not removed. Therefore, we additionally removed patients with more than nine mutations and consequently had a large number of trees. This left us with a data set with $n = 1224$ patients and $m = 406$ mutations. We ran CloMu with default settings and $L = 5$ hidden neurons. Our RL algorithm took <5 h to train the neural network on a laptop with a 2.4-GHz CPU and 64 GB of RAM without using a GPU.

On the task of determining mutation fitness, we found that only eight mutations have high fitness values (>0.003) as shown in Figure 3A. Specifically, the highest fitness mutation was determined to be *TP53*, a known tumor-suppressor gene (Hollstein et al. 1991). The clone with only *TP53* had a fitness (0.0125) over five times the median fitness value (0.00234). Additionally, in order, the next highest fitness mutations were determined to be *CDH1*, *PIK3CA*, *GATA3*, and *MAP3K1*, with fitness values between 0.00658 and 0.0104. Finally, the third tier consists of *ARID1A*, *ESR1*, and *KMT2C* with fitness values between 0.00384 and 0.00440. All of these are known driver mutations (Sondka et al. 2018).

On the task of determining interchangeability and shared mutation properties, we inspected the latent representations of all mutations. We found five mutations with significant magnitude latent representations, corresponding to the five highest fitness mutations: *CDH1*, *GATA3*, *MAP3K1*, *PIK3CA*, and *TP53*. Among these mutations, we found two pairs of interchangeable mutations (Fig. 3B). First, *CDH1* and *PIK3CA* had similar latent representations, with similar values (0.580 and 0.491, respectively) in the first component and values of roughly zero (magnitude under 0.03) in the other components. Second, *GATA3* and *MAP3K1* have similar latent representations, with similar values (0.334 and 0.233, respectively) in the first component and values of roughly zero (magnitude under 0.001) in the other components. In fact, the only high-fitness mutation that our model determined to be highly unique is *TP53*. We found *TP53* to have a separate property expressed by having a different dimension in its latent representation unseen by other mutations (corresponding to the second component). In Supplemental Material C.1.2 and Supplemental Figure S25, these latent representations are also shown to be associated with the hormone receptor status of the breast cancer patient. Additionally, Supplemental Figures S26 and S27 further analyze the latent representations and their association with fitness.

Finally, we analyzed relative causality among the five highest-fitness mutations. Recall that a relative causality value $R(s, t)$ significantly greater than zero is indicative of mutation s causing mutation t in the same clone, whereas a value significantly smaller than zero is indicative of mutation s inhibiting the occurrence of mutation t in the same clone (see section "Prediction tasks"). We identified more negative (11 pairs) than positive (six pairs) causal relationships between pairs (s, t) of mutations (Fig. 3C). This indicates that high-fitness mutations, or drivers, increase the

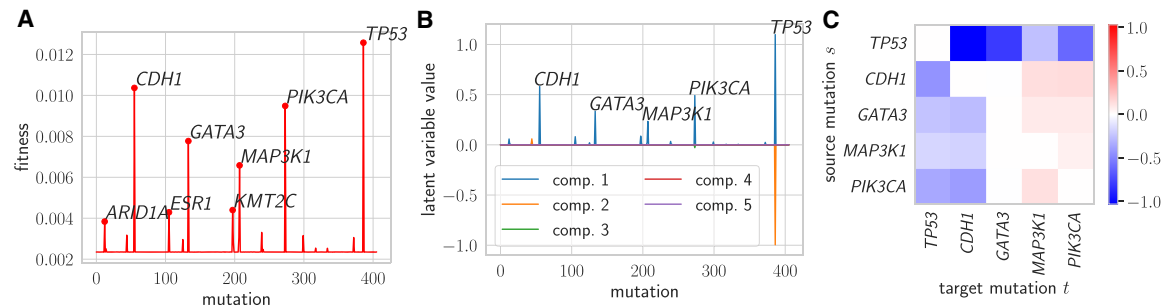


Figure 3. CloMu determines mutation fitness, uncovers mutation similarity, and interchangeability, and finds relative causal relationships on a breast cancer cohort (Razavi et al. 2018). (A) CloMu identified eight mutations that have a far greater fitness value than other mutations. (B) Among these eight mutations, five mutations had latent representations with significant nonzero magnitudes. This plot shows that *CDH1* and *PIK3CA*, as well as *GATA3* and *MAP3K1*, are interchangeable on these data. (C) Relative causal relationships between mutation pairs (s , t). A value greater than zero (red) is indicative of mutation s (row) causing mutation t (column) in the same clone, whereas a value smaller than zero (blue) is indicative of mutation s inhibiting the occurrence of mutation t in the same clone.

likelihood of passenger mutations by more than they increase the likelihood of other driver mutations. This is especially the case for *TP53*, which has a median relative causality value of the seven other highest-fitness mutations versus a relative causality value of 0.476 for the remaining mutations. Among the positive causal relationships, we found that *CDH1* and *GATA3* both cause *PIK3CA*. This is in agreement with TreeMHN's conclusions that *CDH1* causes *PIK3CA* and that there is some level of co-occurrence between *GATA3* and *PIK3CA* (Luo et al. 2023).

To summarize, CloMu agrees with TreeMHN on many causal relationship predictions while also producing interchangeable mutation predictions and fitness predictions that match known driver mutations. We assessed the confidence of our mutation fitness and causality predictions using bootstrapping in Supplemental Material C.1.1 and Supplemental Figures S22 through S24, finding that our predictions are stable across bootstrapped instances. A more systematic comparison of the causal relationship predictions of CloMu and TreeMHN is provided in Supplemental Material C.1.3 and Supplemental Table S3, showing that CloMu and TreeMHN fully agree on a subset of mutation pairs in which one would expect agreement despite our definition differences. We note that, unlike our simulations (Supplemental Material B.3.11), we did not detect any evidence of nonlinear multimutation causality. Finally, we tested CloMu's ability to predict subsequent mutations on subtrees (as explained in Supplemental Fig. S28) in Supplemental Material C.1.4 and Supplemental Figure S29, showing accuracy beyond baseline methods.

CloMu identifies orthogonally validated fitness values in an acute myeloid leukemia cohort

We analyzed a cohort of 123 acute myeloid leukemia (AML) patients that underwent high-throughput single-cell DNA panel sequencing (Morita et al. 2020). Because of the relatively small number of patients, we only analyzed the gene-level data with the exception of the gene *FLT3*, for which we additionally distinguished an internal tandem duplication mutation in *FLT3* denoted as *FLT3-ITD*. We used the phylogenies inferred by Morita et al. (2020) using SCITE (Jahn et al. 2016). We restricted our analysis to the 77 patients with reported clonal prevalences. Again, for training efficiency reasons for our particular RL implementation (Supplemental Material A.1.4), we removed patients with more than 10 mutated genes. We arrived at $n=75$ patients with $m=22$ total mutated genes. One reason we chose to analyze this data

set is that it includes clonal prevalence data, an independent source of fitness information that we used for orthogonal validation of our fitness predictions. Because we collapsed mutations to the gene level, we disabled the infinite sites mode in CloMu. We used default parameters with $L=5$ hidden neurons. Training the neural network took <1 h on a laptop with a 2.4-GHz CPU and 64 GB of RAM without using a GPU.

We used CloMu to predict mutation fitness, interchangeability, and causality. Our model determined the most fit mutations to be *NPM1* and *DNMT3A*, with fitness values of 0.338 and 0.184 relative to a median fitness of 0.019 (Fig. 4A). *NPM1* and *DNMT3A* are well-known driver mutations for AML (Sondka et al. 2018). Corroborating our finding, TreeMHN determined the *DNMT3A* mutation to cause the largest number of other mutations (eight pairs) while only inhibiting one mutation. In addition, CloMu determined mutations *ASXL1*, *GATA2*, and *U2AF1* to have high fitness, with values ranging from 0.0394 to 0.0546. On the other hand, we found that *FLT3* had a below median fitness of 0.00585. This matches the fact that TreeMHN determined *FLT3* to have the largest number of strong negative causal relationships (three pairs).

To confirm the validity of our fitness predictions, we investigated the clone prevalence data that we did not use for training CloMu. Specifically, for each patient p and mutation s , let $\gamma_1(p, s)$ be the prevalence of the clone in which mutation s was introduced. Additionally, let $\gamma_0(p, s)$ be the prevalence of the parent clone of the clone in which mutation s was introduced. We define the *log prevalence ratio* as $\Gamma(p, s) = \log((\gamma_1(p, s) + 0.01)/(\gamma_0(p, s) + 0.01))$, which adds 0.01 to all prevalence measurements in order to avoid issues caused by dividing by or taking the log of very low numbers. Intuitively, if mutation s is highly fit, it should cause the clone that introduced mutation s to outgrow its parent clone, which would lead to a positive value for $\Gamma(p, s)$. Conversely, a mutation s that does not increase the fitness of the clone that introduced it would lead to a nonpositive $\Gamma(p, s)$. We analyzed the eight mutations with the lowest standard error in their $\Gamma(p, s)$ measurements. Three of these mutations (*DNMT3A*, *ASXL1*, and *NPM1*) were determined to be highly fit by our model, and five were determined to have low fitness (*IDH1*, *FLT3-ITD*, *PTPN11*, *NRAS*, and *FLT3*). The log prevalence ratio measurements agreed with our model's conclusion on all eight mutations (Fig. 4B). In fact, the one mutation, *FLT3*, that our model predicted to have below median fitness also was determined to have the smallest median log prevalence ratio of -0.888 . We further investigated the association between fitness and prevalence in Supplemental

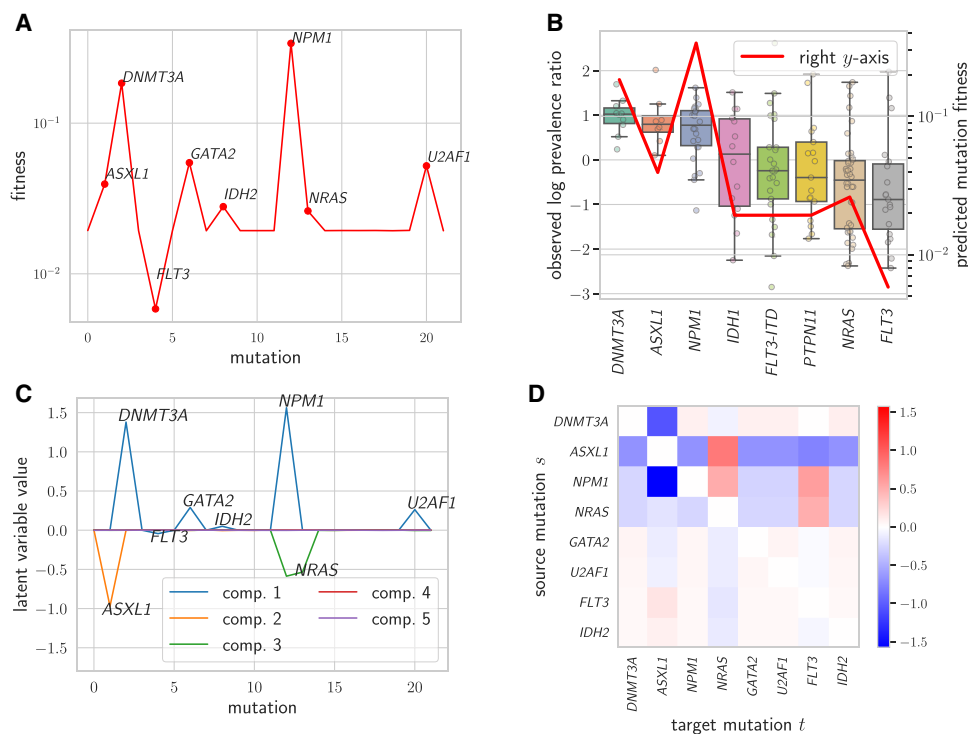


Figure 4. CloMu predicts fitness values validated by clone prevalence measurements and uncovers interchangeability and relative causal relationships on an AML data set (Morita et al. 2020). (A) CloMu identifies seven mutations with far greater fitness values than other mutations and identified one mutation (*FLT3*) with a substantially lower fitness value. (B) Box plot of log prevalence ratios for the eight mutations with the low standard error in log prevalence ratios (left y-axis), as well as a line showing our predicted mutation fitness values (right y-axis). The results show the validity of our fitness predictions. (C) Latent representations of mutations obtained from the $L=5$ hidden neurons. This plot shows that *GATA2* and *U2AF1* are interchangeable on these data. (D) Relative causal relationships between mutation pairs (s, t). A value greater than zero (red) is indicative of mutation s (row) causing mutation t (column) in the same clone, whereas a value smaller than zero (blue) is indicative of mutation s inhibiting the occurrence of mutation t in the same clone.

Material C.2.1 and Supplemental Figures S30 and S31 to ensure the validity of these results. Briefly, we found that although our method may have diminished sensitivity in detecting high fitness mutations that typically occur terminally, we believe that specificity is not affected by mutation timing.

CloMu also analyzed shared properties and interchangeability of mutations. We found *GATA2* and *U2AF1* to be interchangeable with similar latent representations (Fig. 4C). Additionally, we found *NPM1* and *DNMT3A* to have shared properties. Specifically, the first dimension of their latent representation is nearly identical (shown in blue in Fig. 4C). However, *NPM1* also has a shared property in the third latent dimension (shown in green in our plot), which is not present in *DNMT3A*. Finally, *ASXL1* was determined to be completely unique, using the second dimension in its latent representation (shown in orange in our plot) unlike any other mutation. These patterns of interchangeability were also reflected in the causality relationships identified by CloMu (Fig. 4D). We provide additional plots and analyses of these latent representations in Supplemental Material C.2.2, Supplemental Figures S32 and S33.

The two main positive causal relationships found are from *ASXL1* and *NPM1* to *NRAS*—with $R(\text{ASXL1}, \text{NRAS})=0.814$ and $R(\text{NPM1}, \text{NRAS})=0.505$ (Fig. 4D). TreeMHN agrees with our conclusion that *NPM1* causes *NRAS*. Although GeneAccord detects the co-occurrence of *NPM1* and *NRAS*, the method does not have the capability to identify the directionality causal relationships. In our model, we found the strongest negative causal relationship to be from *NPM1* to *ASXL1*, namely, $R(\text{NPM1}, \text{ASXL1})=-1.57$. In addition, we identified a strong negative causal relationship in the

reverse direction, namely, $R(\text{ASXL1}, \text{NPM1})=-0.667$. Such bidirectional negative causality is indicative of mutual exclusivity. Indeed, TreeMHN also identified this bidirectional negative causal relationship. Mutual exclusivity between *ASXL1* and *NPM1* has been described previously in the literature (Pratcorona et al. 2012). Moreover, a strong negative association from *ASXL1* to *FLT3-ITD* has also been reported (Pratcorona et al. 2012). Indeed, CloMu identified a strong negative causal relationship from *ASXL1* to *FLT3-ITD* ($R(\text{ASXL1}, \text{FLT3-ITD})=-0.754$ and $R(\text{FLT3-ITD}, \text{ASXL1})=0.131$). CloMu thus determines known causal relationships not picked up by other methods while also producing orthogonally validated fitness predictions. For a more systematic comparison of the causal relationship predictions of CloMu and TreeMHN, see Supplemental Material C.2.3 and Supplemental Table S4. We did not detect any evidence of nonlinear multimutation causality in this data set. Finally, we evaluated CloMu's ability to predict subsequent mutations on subtrees of these data in Supplemental Material C.2.4 and Supplemental Figure S34.

Discussion

In this work, we introduced CloMu, a tree generative model of cancer evolution, which can be used to perform tree selection; determine mutation fitness, causality, and interchangeability; and detect complex evolutionary pathways composed of sets of interchangeable mutations. Like TreeMHN (Luo et al. 2023) and HINTRA (Khakabimamaghani et al. 2019), CloMu models the generation of trees by independently determining the rate of new

mutations occurring on a clone based on the clone's current mutations. CloMu uses a low-parameter neural network, which affords it the flexibility to model complex multimutation interactions while retaining resistance to overfitting. Using simulations without interchangeable mutations, we showed that CloMu matches TreeMHN's performance and outperforms all other baseline methods for the task of detecting causal relationships. Additionally, in the presence of interchangeable mutations, CloMu greatly outperformed TreeMHN as well. Our simulations further showed CloMu's accuracy in performing tree selection and identifying interchangeable mutations and their evolutionary pathways, outperforming competing methods. On real cancer data consisting of a breast cancer cohort (Razavi et al. 2018) and an AML cohort (Morita et al. 2020), CloMu was able to assess mutation fitness, determine interchangeable mutations and find causal relationships. We found that mutations with high fitness typically correspond to known driver mutations and that causal relationships matched previously reported associations and patterns of mutual exclusivity. For the AML data, we performed additional orthogonal validation by comparing predicted mutation fitness values to the prevalences of clones, finding high consistency. These findings show that CloMu is a versatile and effective method for a wide variety of prediction tasks regarding cancer evolution.

There are several directions for future work and expansions of CloMu. First, a limitation of our method is how sampling time affects our predictions. In practice, the time at which the tumor is sampled is nonrandom. If some mutation greatly increases the severity of the tumor as well as symptoms, the patient is more likely to have the tumor sequenced at this time. Consequently, if a clone is sufficiently severe, it may result in the tumor being sequenced before that clone has had time to acquire additional mutations (thus leading to lower fitness per our definition). Such a terminal clone may have high clonal prevalence, a signal that is not used by the model. Thus, beyond only considering tree topology and mutation placement, one could incorporate cancer progression models that incorporate measurements of clonal prevalences to improve predictions (Beerenwinkel et al. 2015). Second, one could use CloMu's low-dimensional representations of clones and mutations to predict measured properties of cancer clones or mutations, such as response to treatment or other patient outcomes. Third, one could extend CloMu's model to support somatic mutations beyond SNVs such as copy-number aberrations (CNAs) and their interplay with SNVs, including mutation loss. Fourth, one could improve CloMu's computational efficiency on data sets with large numbers of mutations per patient and vast numbers of possible trees per patient, especially when including mutations beyond SNVs such as CNAs. We note that to keep runtimes manageable, our present analyses restricted the number of SNVs per patient on real data sets. Fifth, the effects of germline predispositions can be captured by encoding them in the same way as mutations, that is, including an additional predisposition-specific "mutation" at the root node followed by the rest of the original tree. Similarly, one could encode therapeutics as occurring on all clones at the same time in the same way as mutations are encoded. Encoding such events in the input trees will enable the model to learn their downstream effects on future mutations. Sixth, we only evaluated multimutation effects on simulated data, which required a large number $n \approx 500$ of patients and large effect sizes. Our simulations showed that it is feasible to detect complex patterns such as two mutations s and t only causing a third mutation r when paired together. Additionally, because of limited cohort sizes, we collapsed mutations in the real data to the gene level and

only retained frequently recurrent genes, preventing the detection of mutation-specific patterns or the effects of rare genes. To perform more detailed analyses on real data in future work, we require much larger data sizes than currently available, which we expect to see in the future.

Methods

Independent clonal evolution problem

As previously stated, we take as input a set of possible tumor phylogeny trees $\{T_1, \dots, T_{|T_p|}\}$ for each patient p among a cohort of n patients with m total mutations. Additionally, we have assumed independent clonal evolution. Although clonal cooperation has been described in the literature (Tabassum and Polyak 2015; Kuipers et al. 2021), the resulting problem under our assumption still enables meaningful analyses even for cases with violations to this assumption (Supplemental Material B.3.6). Our function, $f_\theta: \{0, 1\}^m \times [m] \rightarrow \mathbb{R}$, outputs the logarithm of the rate at which the mutation occurs on the clone (Fig. 1A). As such, the probability of mutation s occurring on the clone \mathbf{c} in the next δ time units is $\delta \exp(f_\theta(\mathbf{c}, s))$ for small δ . Our trees are generated by iteratively building upon partial trees starting with the tree $T^{(0)}$ with only a single normal clone $\mathbf{c}_0 = [0, \dots, 0]^T$. Given a tree $T^{(k)}$ with clones $C^{(k)} = [\mathbf{c}_0, \dots, \mathbf{c}_k]^T$, the conditional probability $\Pr((\mathbf{c}_i, s) | \mathbf{c}_0, \dots, \mathbf{c}_k, f_\theta)$ of the next mutation s to occur on clone \mathbf{c}_i among clones $C^{(k)}$, denoted by (\mathbf{c}_i, s) , equals

$$\Pr((\mathbf{c}_i, s) | \mathbf{c}_0, \dots, \mathbf{c}_k, f_\theta) = \exp(f_\theta(\mathbf{c}_i, s)) / \sum_{j=0}^k \sum_{t=1}^m \exp(f_\theta(\mathbf{c}_j, t)). \quad (1)$$

This yields a new tree $T^{(k+1)}$ with a new clone \mathbf{c}_{k+1} with \mathbf{c}_i as its parent. Equivalently, we may represent the conditional probability density function with a softmax as $P = [p_{0,1}, \dots, p_{k,m}]^T = \text{softmax}([f_\theta(\mathbf{c}_0, 1), \dots, f_\theta(\mathbf{c}_k, m)]^T)$ where $p_{i,s} = \Pr((\mathbf{c}_i, s) | \mathbf{c}_0, \dots, \mathbf{c}_k, f_\theta)$ (see Fig. 1B). Importantly, we assume mutations are irreversible as clones can only be modified by adding additional mutations. Optionally, the infinite site assumption can be enforced by setting the probabilities $p_{0,s}, \dots, p_{k,s}$ of a new mutation s to zero if mutation s already exists in one of the clones $\mathbf{c}_0, \dots, \mathbf{c}_k$. We terminate the tree generation process when we reach a prespecified number $\ell \leq m$ of mutations.

As stated in the INDEPENDENT CLONAL EVOLUTION problem, our goal is maximizing the probability of observing the input data. Thus, we must describe exactly how to define the probability $\Pr(T | f_\theta)$ of any tree T . However, there are multiple possible ways of generating each tree. For example, consider the tree T with $\ell = 2$ mutations having the normal clone \mathbf{c}_0 as the root with two children: a clone with mutation 1 and a clone with mutation 2. There are two ways to generate T , either mutation 1 or mutation 2 could occur first on \mathbf{c}_0 followed by the other mutation, namely, $(\mathbf{c}_0, 1), (\mathbf{c}_0, 2)$ or $(\mathbf{c}_0, 2), (\mathbf{c}_0, 1)$. We refer to a specific way of generating a tree T with ℓ mutations as a *tree generating process* G , which is an ordered list $(\mathbf{c}_0, s_{i_0}), (\mathbf{c}_{i_1}, s_{i_1}), \dots, (\mathbf{c}_{i_{\ell-1}}, s_{i_{\ell-1}})$, where each pair indicates the source clone and the mutation that was added to it. Using the independent clonal evolution assumption, we can now express the probability of a tree generating process $G = (\mathbf{c}_0, s_{i_0}), (\mathbf{c}_{i_1}, s_{i_1}), \dots, (\mathbf{c}_{i_{\ell-1}}, s_{i_{\ell-1}})$ as

$$\Pr(G | f_\theta) = \prod_{k=0}^{\ell-1} \Pr((\mathbf{c}_{i_k}, s_{i_k}) | \mathbf{c}_0, \dots, \mathbf{c}_{k-1}, f_\theta). \quad (2)$$

We denote the set of all tree generating processes that yield a tree T by $\mathcal{G}(T)$ such that $\Pr(T | f_\theta) = \sum_{G \in \mathcal{G}(T)} \Pr(G | f_\theta)$. As tumors are separate evolutionary processes, we have independence across patients

and can therefore express the probability of our data as

$$\begin{aligned} \Pr(\mathcal{T}_1, \dots, \mathcal{T}_n | f_\theta) &= \prod_{p=1}^n \sum_{T \in \mathcal{T}_p} \Pr(T | f_\theta) \\ &= \prod_{p=1}^n \sum_{T \in \mathcal{T}_p} \sum_{G \in \mathcal{G}(T)} \Pr(G | f_\theta). \end{aligned} \quad (3)$$

We note that HINTRA (Khakabimamaghani et al. 2019) and TreeMHN (Luo et al. 2023) solve the INDEPENDENT CLONAL EVOLUTION problem with different types of models (Table 2). The function f_θ used by HINTRA explicitly enumerates all $2^m \times m$ clone–mutation pairs. The advantage of HINTRA’s model is its flexibility to fit any pattern of clone-to-mutation interactions, but this comes at the expense of severely restricting its scalability to a small number of mutations. On the other hand, TreeMHN defines f_θ using a linear model of additive rate coefficients for all $m \times m$ pairs of mutations. As we showed in the section “Benchmarking on simulated data,” this scales well but does not capture nonadditive clone-to-mutation interactions nor shared properties of mutations such as two mutations similarly affecting the probability of other mutations. As discussed in the section “CloMu: low-parameter neural network trained via reinforcement learning,” in our method CloMu, the model f_θ is a two-layer neural network with $L = 5 \ll m$ hidden neurons (Fig. 1C). The small number of parameters and the ability to model nonadditive clone-to-mutation interactions lead CloMu to achieve flexibility like HINTRA while also being more resistant to overfitting than either TreeMHN or HINTRA on data sets with a large number of mutations. Beyond the model type, there are other subtle differences. Rather than considering the set $\mathcal{G}(T)$ of all tree generative processes of a tree T , HINTRA considers a single tree generative process G to compute the probability of T .

Prediction tasks

We gave a brief description of the prediction task in the Results. These prediction tasks are elaborated on and defined more precisely here. Importantly, these prediction tasks correspond to postprocessing the model f_θ learned only once for each data set $\{\mathcal{T}_1, \dots, \mathcal{T}_n\}$.

Reducing phylogeny uncertainty can be accomplished by selecting trees $T \in \mathcal{T}_p$ with a high value of $\Pr(T | f_\theta)$ for each patient p (Fig. 1D). To select a single tree per patient, one can simply choose the tree T that maximizes $\Pr(T | f_\theta)$.

For determining the fitness of mutations, we consider the set $\{\mathbf{c}_1, \dots, \mathbf{c}_m\}$ of clones in which each clone \mathbf{c}_s consists of only mutation s . Intuitively, the fitness of a clone \mathbf{c}_s and, consequently, mutation s is proportional to the rate at which a mutation would occur on the clone (Fig. 1E). As such, normalizing this over all clones $\mathbf{c}_1, \dots, \mathbf{c}_m$ yields the expression of *mutation fitness* F_s for mutations s :

$$F_s = \sum_{t=1}^m \exp(f_\theta(\mathbf{c}_s, t)) / \sum_{i=1}^m \sum_{t=1}^m \exp(f_\theta(\mathbf{c}_i, t)). \quad (4)$$

As an example, if the fitness F_s of mutation s is 10 times larger than the fitness F_t of mutation t , this implies mutations occur on the clone \mathbf{c}_s at a rate that is 10 times higher than the rate at which new mutations occur on the clone \mathbf{c}_t . Although the fitness value is defined only in terms of clones with a single mutation, we typically expect the fitness value to generalize such that on all clones, having mutation s rather than t will increase the rate of new mutations occurring. Additionally, our fitness definition assumes that an increasing rate of mutations on a clone is associated with clonal expansion. However, there exist some exceptions to this assumption. For instance, mutations that interfere with DNA mismatch repair mechanisms may increase the rate of mutations, and thus, our

definition may overestimate their fitness. That is, unless there is specific evidence of nonlinear effects of combinations of mutations in the data set, our regularized neural network model would naturally predict the same linear effect of a mutation on the rates of all other mutations for all clones. In cases with such nonlinear effects, assigning a single fitness value to a mutation will not capture these effects. An important note is that our fitness predictions for a mutation s are entirely learned based on the occurrence of additional mutations in clones with mutation s in the phylogeny. As such, if mutation s is always terminal, our model would not be able to conclude s to be high fitness. This is an intrinsic limitation of only using tree data but could be addressed by incorporating additional information such as clonal prevalence values.

We determine causal relationships between pairs of mutations. By causal relationships, we mean temporal patterns of co-occurrence and mutual exclusivity on a clonal level in the context of phylogenetic tree. Under our simplified model of clonal evolution, these patterns are causal. However, the biology of clonal evolution is too complex to know definitively if they are causal or simply correlative in the true biological system of clonal evolution. We define *absolute causality* as

$$A(s, t) = f_\theta(\mathbf{c}_s, t) - f_\theta(\mathbf{c}_0, t), \quad (5)$$

namely, the log ratio of rates of mutation t occurring on clone \mathbf{c}_s versus clone \mathbf{c}_0 (Fig. 1F). Recall that $f_\theta(\mathbf{c}, s)$ is the logarithm of the rate at which a mutation s occurs on clone \mathbf{c} . In practice, some threshold value $\tau > 0$ in the strength of the causal relationship must be used in order to avoid false positives. Therefore, for absolute causality, we say s *causes* t if $f_\theta(\mathbf{c}_s, t) - f_\theta(\mathbf{c}_0, t) > \tau$, s *inhibits* t if $f_\theta(\mathbf{c}_s, t) - f_\theta(\mathbf{c}_0, t) < -\tau$, and there is no causal relationship from s to t otherwise. Note that causality is bidirectional, namely, we can assess causality from t to s by evaluating $f_\theta(\mathbf{c}_t, s) - f_\theta(\mathbf{c}_0, s)$, amounting to a total of nine possible pairs of causal relationships between any two mutations. One potential issue with absolute causality is that a high fitness mutation s may increase the rates of all other mutations $t \neq s$ and thus have a positive causal relationship with all other mutations t . To address this issue, we define *relative causality* $R(s, t)$ from s to t as

$$R(s, t) = \log \left[\frac{\exp(f_\theta(\mathbf{c}_s, t)) / \sum_{r=1}^m \exp(f_\theta(\mathbf{c}_s, r))}{\frac{1}{m} \sum_{q=1}^m (\exp(f_\theta(\mathbf{c}_q, t)) / \sum_{r=1}^m \exp(f_\theta(\mathbf{c}_q, r)))} \right]. \quad (6)$$

This measures how much a mutation s increases the relative probability that t will be the next mutation to occur on the clone, relative to the average of all clones \mathbf{c}_q with one mutation q . As an example, consider three mutations s, t , and r such that $R(s, t) = R(r, t) + x$. Then the probability that the next mutation is t on a clone that already has s is $\exp(x)$ times larger than the probability that the next mutation is t on a clone that already has r . Let 0.1 be the probability that the next mutation on a clone with r is mutation t . Also, let $x = \log_2$. An example further showing relative and absolute causality is provided in Supplemental Table S1. Then the probability of the next mutation on a clone with s being mutation t is $\exp(\log_2) \cdot 0.1 = 0.2$. Similarly to absolute causality, we say s *causes* t if $R(s, t) > \tau$, s *inhibits* t if $R(s, t) < -\tau$, and there is no causal relationship from s to t otherwise. In general, one should use absolute causality if one simply wants to know if having mutation s increases the rate of mutation t occurring for any reason including mutation s being high fitness. Alternatively, one should use relative causality if one wants to know if there is a specific relationship between s and t such that s increases the likelihood of t occurring relative to all other mutations. Additionally, we define

multimutation causality to capture the nonlinear effect of a combination of multiple mutations causing some other mutation (Supplemental Material A.2.2).

There is an extensive body of work on identifying mutations that are mutually exclusive or co-occur (Leiserson et al. 2015; Dao et al. 2017; Kim et al. 2017; Kuipers et al. 2021). Briefly, mutations in genes in the same biological pathway tend to be mutually exclusive as any individual mutation dysregulates the same pathway (Yeang et al. 2008). On the other hand, some mutations tend to co-occur as their simultaneous presence might be beneficial for cancer progression (Muzny et al. 2012; Wang et al. 2014; Hill et al. 2015; Ulz et al. 2016). Although many previous works have focused on identifying such mutations at the patient level without directly considering their effects on subsequent mutations, here we seek to identify interchangeable mutations that have similar impacts on subsequent mutation evolution. That is, we define two mutations $s \neq t$ to be *interchangeable* if it holds that $f_{\theta}(\mathbf{c}, r) \approx f_{\theta}(\mathbf{c}', r)$ for all mutations $r \in [m] \setminus \{s, t\}$ and for any two clones \mathbf{c} and \mathbf{c}' that are identical except for \mathbf{c} containing mutation s but not t , and vice versa for \mathbf{c}' (Fig. 1G). Note that this definition does not constrain the causal relationship among s and t . If s and t are interchangeable and pairwise inhibitory, this could be a result of them belonging to the same functional pathway. Conversely, if s and t are interchangeable and co-occur, it could be a result of s and t having an additive effect when simultaneously present. The probability $f_{\theta}(\mathbf{c}, r)$ for all r is entirely determined by the values of the hidden neurons of our neural network when \mathbf{c} is taken as an input. Consequently, two clones \mathbf{c} and \mathbf{c}' behave identically according to our model if their latent representations (hidden neuron values) are identical. Thus, the clone \mathbf{c}_s with only mutation s and the clone \mathbf{c}_t with only mutation t behave identically if they have identical latent representations. Rather than comparing the latent representations on vast numbers of pairs of clones differing by one mutation, we define the latent representation of a mutation s as the latent representation of the clone \mathbf{c}_s and predict two mutations to be interchangeable if their latent representations are very close in terms of Euclidean distance.

A *pathway of interchangeable mutations* requires that mutations in some set A and some set B are required together in order to increase the likelihood of mutations in some set C (Fig. 1H). Mathematically, if $t \in A$, $s \in B$, and $r \in C$, this implies $f_{\theta}(\mathbf{c}_s, r) \approx f_{\theta}(\mathbf{c}_0, r) \approx f_{\theta}(\mathbf{c}_t, r)$ and $f_{\theta}(\mathbf{c}_{st}, r) > f_{\theta}(\mathbf{c}_0, r)$, where \mathbf{c}_{st} is the clone that contains only mutations s and t . Note that the case in which each set consists of a single mutation, namely, $|A| = |B| = |C| = 1$, corresponds to multimutation causality (for discussion, see Supplemental Material A.2.2). For a detailed description on how we infer pathways of interchangeable mutations, see Supplemental Material A.2.1. A final prediction task is the inference of consensus trees, which are a small number of trees that best summarize the diversity of trees in the cohort (Supplemental Material A.2.3). Finally, we use bootstrapping to assess confidence of CloMu's predictions (Supplemental Material A.3).

CloMu: low-parameter neural network trained via reinforcement learning

CloMu uses a two-layer neural network with a small number L of hidden neurons for the function f_{θ} (Fig. 1C). This model has $2Lm + m + L = O(Lm)$ total parameters. In experiments in this paper, we use $L = 5$ hidden neurons. As the number of parameters grows linearly in the number of mutations, this model is very resistant to overfitting. Moreover, we made a slight modification to the neural network to allow for easier regularization, which is used primarily for the sake of interpretability but also is used to avoid overfitting on some extremely small data sets. This modification

did not affect the scaling of the number parameters. For more details, see Supplemental Material A.1.1.

The small number L of hidden neurons allows us to form a small L -dimensional representation of any input clone \mathbf{c} . Applying this to the set $\{\mathbf{c}_1, \dots, \mathbf{c}_m\}$ of clones with only one mutation, we obtain *latent representations* $\mathbf{l}_t = [l_1, \dots, l_L] \in \mathbb{R}^L$ for each mutation $t \in [m]$ by observing the values of the L hidden neurons given the clone \mathbf{c}_t . The latent representation encapsulates any effect the mutation could have on some clone according to the model, and thus, similarity of two latent representations also indicates similarity between the two mutations. In practice, we use the Euclidean distance $\|\mathbf{l}_s - \mathbf{l}_t\|_2$ between latent representations to determine the interchangeability of any pair (s, t) of mutations. For the sake of interpretability, we subtract the median value across all mutations from each component of each latent representation.

For the task of modeling evolutionary pathways of interchangeable mutations, it is vital to understand when two mutations are required together in order to cause a third mutation. Having a nonlinear model such as our neural network is thus required for this task. Specifically, we find evolutionary pathways of interchangeable mutations through the following, which is described extensively in Supplemental Material A.2.1. First, we evaluate the probability of the tumor evolving in some evolutionary pathway according to our model. Then, we evaluate the probability of the tumor evolving in that same pathway under a null hypothesis in which mutations have no effect on clonal evolution. Finally, we search for evolutionary pathways in which the probability according to our model vastly exceeds the null hypothesis probability.

The sets $\mathcal{T}_1, \dots, \mathcal{T}_n$ and especially $\mathcal{G}(T)$ can be very large. For instance, if T is the star tree in which 10 mutations are made on the root node, $\mathcal{G}(T)$ will have $10! = 3,628,800$ elements. Explicitly calculating $\Pr(G|f_{\theta})$ for every $G \in \mathcal{G}(T)$ and $T \in \mathcal{T}_p$ can be infeasible. To avoid doing this, we use reinforcement learning to train the neural network, that is, infer model parameters θ that maximize the likelihood of the data. Note that the use of reinforcement learning is a standard approach for training neural networks (François-Lavet et al. 2018). We use policy gradients, adapting the REINFORCE method (Williams 1992), in which the model is given a reward when it generates a tree in the data set. Specifically, the reward is proportional to how much increasing the probability of that tree would increase the overall log probability of our data set. Typically, in reinforcement learning, the reward given to the model for a given action sequence is independent of the model itself. In our case, in order to maximize the probability of observing the data, our reward is a function that depends on the model. However, to correctly optimize our objective, the rewards must be treated only as numerical values, and the gradient of the reward must not be taken with respect to the parameters. Although it is less common to have a changing reward function during training, there exist other examples of this in the reinforcement learning literature. One such example is curiosity driver exploration in which the intrinsic reward changes during training (Pathak et al. 2017). Another such example is maximum entropy gain exploration, in which entropy is maximized in addition to maximizing total rewards (Pitis et al. 2020). In CloMu, as well as these papers, the reward changes based on how the probability of states/actions change owing to the policy changing during training. As is typical, our model is trained via stochastic gradient descent on the typical policy gradient's loss function. Additionally, we have modified our sampling procedure to increase training speed and accuracy in the case that there are moderately few trees per patient and consequently adjusted the reward function. For more details, see Supplemental Material A.1.4.

We implemented CloMu in Python 3 using the PyTorch library. CloMu is open source and is available at GitHub (<https://github.com/elkebir-group/CloMu>).

Software availability

The code for CloMu and the used simulated and real data are available at GitHub (<https://github.com/elkebir-group/CloMu>). These are also available as Supplemental Code and Supplemental Data, respectively.

Competing interest statement

The authors declare no competing interests.

Acknowledgments

We thank the Beerenwinkel laboratory and Xiang Ge Luo for providing access to TreeMHN simulation results. This work started as a course project in “CS598MEB: Computational Cancer Genomics.” M.E.-K. was supported by the National Science Foundation (CCF-2046488) as well as funding from the Cancer Center at Illinois.

Author contributions: S.I. and M.E.-K. designed the study. S.I. implemented the method and performed the analyses. S.I. and M.E.-K. interpreted the results and wrote the manuscript.

References

Beerenwinkel N, Schwarz RF, Gerstung M, Markowitz F. 2015. Cancer evolution: mathematical models and computational inference. *Syst Biol* **64**: e1–e25. doi:10.1093/sysbio/syu081

Caravagna G, Giarratano Y, Ramazzotti D, Tomlinson I, Graham TA, Sanguinetti G, Sottoriva A. 2018. Detecting repeated cancer evolution from multi-region tumor sequencing data. *Nat Methods* **15**: 707–714. doi:10.1038/s41592-018-0108-x

Christensen S, Kim J, Chia N, Koyejo O, El-Kebir M. 2020. Detecting evolutionary patterns of cancers using consensus trees. *Bioinformatics* **36**: i684–i691. doi:10.1093/bioinformatics/btaa801

Dao P, Kim YA, Wojtowicz D, Madan S, Sharan R, Przytycka TM. 2017. BeWith: a Between-Within method to discover relationships between cancer modules via integrated analysis of mutual exclusivity, co-occurrence and functional interactions. *PLoS Comput Biol* **13**: e1005695. doi:10.1371/journal.pcbi.1005695

El-Kebir M, Satas G, Oesper L, Raphael BJ. 2016. Inferring the mutational history of a tumor using multi-state perfect phylogeny mixtures. *Cell Syst* **3**: 43–53. doi:10.1016/j.cels.2016.07.004

François-Lavet V, Henderson P, Islam R, Bellemare MG, Pineau J. 2018. An introduction to deep reinforcement learning. *Found Trends Mach Learn* **11**: 219–354. doi:10.1561/22000000071

Hanahan D, Weinberg RA. 2000. The hallmarks of cancer. *Cell* **100**: 57–70. doi:10.1016/S0092-8674(00)81683-9

Hill RM, Kuijper S, Lindsey JC, Petrie K, Schwalbe EC, Barker K, Boulton JK, Williamson D, Ahmad Z, Hallsworth A, et al. 2015. Combined MYC and P53 defects emerge at medulloblastoma relapse and define rapidly progressive, therapeutically targetable disease. *Cancer Cell* **27**: 72–84. doi:10.1016/j.ccr.2014.11.002

Hodzic E, Shrestha R, Malikic S, Collins CC, Litchfield K, Turajlic S, Sahinalp SC. 2020. Identification of conserved evolutionary trajectories in tumors. *Bioinformatics* **36**: i427–i435. doi:10.1093/bioinformatics/btaa453

Hollstein M, Sidransky D, Vogelstein B, Harris CC. 1991. p53 mutations in human cancers. *Science* **253**: 49–53. doi:10.1126/science.1905840

Jahn K, Kuipers J, Beerenwinkel N. 2016. Tree inference for single-cell data. *Genome Biol* **17**: 86. doi:10.1186/s13059-016-0936-x

Kalantari J, Nelson H, Chia N. 2020. The unreasonable effectiveness of inverse reinforcement learning in advancing cancer research. In *The Thirty-Fourth AAAI Conference on Artificial Intelligence, AAAI 2020, The Thirty-Second Innovative Applications of Artificial Intelligence Conference, IAAI 2020, The Tenth AAAI Symposium on Educational Advances in Artificial Intelligence, EAAI 2020*, New York, February 7–12, 2020, pp. 437–445. AAAI Press.

Khakabimamaghani S, Malikic S, Tang J, Ding D, Morin R, Chindelevitch L, Ester M. 2019. Collaborative intra-tumor heterogeneity detection. *Bioinformatics* **35**: i379–i388. doi:10.1093/bioinformatics/btz355

Kim YA, Madan S, Przytycka TM. 2017. WeSME: uncovering mutual exclusivity of cancer drivers and beyond. *Bioinformatics* **33**: 814–821. doi:10.1093/bioinformatics/btw242

Kuipers J, Moore AL, Jahn K, Schraml P, Wang F, Morita K, Futreal PA, Takahashi K, Beisel C, Moch H, et al. 2021. Statistical tests for intra-tumour clonal co-occurrence and exclusivity. *PLoS Comput Biol* **17**: e1009036. doi:10.1371/journal.pcbi.1009036

Leiserson MD, Wu HT, Vandin F, Raphael BJ. 2015. CoMet: a statistical approach to identify combinations of mutually exclusive alterations in cancer. *Genome Biol* **16**: 160. doi:10.1186/s13059-015-0700-7

Luo XG, Kuipers J, Beerenwinkel N. 2023. Joint inference of exclusivity patterns and recurrent trajectories from tumor mutation trees. *Nat Commun* **14**: 3676. doi:10.1038/s41467-023-39400-w

Morita K, Wang F, Jahn K, Hu T, Tanaka T, Sasaki Y, Kuipers J, Loghavi S, Wang SA, Yan Y, et al. 2020. Clonal evolution of acute myeloid leukemia revealed by high-throughput single-cell genomics. *Nat Commun* **11**: 5327. doi:10.1038/s41467-020-19119-8

Muzny DM, Bainbridge MN, Chang K, Dinh HH, Drummond JA, Fowler G, Kovar CL, Lewis LR, Morgan MB, Newsham IF, et al. 2012. Comprehensive molecular characterization of human colon and rectal cancer. *Nature* **487**: 330–337. doi:10.1038/nature11252

Nowell PC. 1976. The clonal evolution of tumor cell populations. *Science* **194**: 23–28. doi:10.1126/science.959840

Pathak D, Agrawal P, Efros AA, Darrell T. 2017. Curiosity-driven exploration by self-supervised prediction. In *Proceedings of the 34th International Conference on Machine Learning, ICML 2017, Sydney, NSW, Australia, 6–11 August 2017*, Vol. 70 of *Proceedings of Machine Learning Research* (ed. Precup D, Teh YW), pp. 2778–2787. PMLR.

Pellegrina L, Vandin F. 2022. Discovering significant evolutionary trajectories in cancer phylogenies. *Bioinformatics* **38**: ii49–ii55. doi:10.1093/bioinformatics/btac467

Pitis S, Chan H, Zhao S, Stadie B, Ba J. 2020. Maximum entropy gain exploration for long horizon multi-goal reinforcement learning. In *Proceedings of the 37th International Conference on Machine Learning, ICML 2020, 13–18 July 2020, Virtual Event*, Vol. 119 of *Proceedings of Machine Learning Research*, pp. 7750–7761. PMLR.

Pratcorona M, Abbas S, Sanders MA, Koenders JE, Kavelaars FG, Erpelinck-Verschueren CA, Zeilemakers A, Löwenberg B, Valk PJ. 2012. Acquired mutations in *ASXL1* in acute myeloid leukemia: prevalence and prognostic value. *Haematologica* **97**: 388–392. doi:10.3324/haematol.2011.051532

Qi Y, Pradhan D, El-Kebir M. 2019. Implications of non-uniqueness in phylogenetic deconvolution of bulk DNA samples of tumors. *Algorithms Mol Biol* **14**: 23–14. doi:10.1186/s13015-019-0155-6

Razavi P, Chang MT, Xu G, Bandlamudi C, Ross DS, Vasan N, Cai Y, Bielski CM, Donoghue MT, Jonsson P, et al. 2018. The genomic landscape of endocrine-resistant advanced breast cancers. *Cancer Cell* **34**: 427–438.e6. doi:10.1016/j.ccr.2018.08.008

Sondka Z, Bamford S, Cole CG, Ward SA, Dunham I, Forbes SA. 2018. The COSMIC Cancer Gene Census: describing genetic dysfunction across all human cancers. *Nat Rev Cancer* **18**: 696–705. doi:10.1038/s41568-018-0060-1

Tabassum DP, Polyak K. 2015. Tumorigenesis: it takes a village. *Nat Rev Cancer* **15**: 473–483. doi:10.1038/nrc3971

Turajlic S, Xu H, Litchfield K, Rowan A, Horswell S, Chambers T, O'Brien T, Lopez JI, Watkins TB, Nicol D, et al. 2018. Deterministic evolutionary trajectories influence primary tumor growth: TRACERx Renal. *Cell* **173**: 595–610.e11. doi:10.1016/j.cell.2018.03.043

Ulz P, Heitzer E, Speicher MR. 2016. Co-occurrence of *MYC* amplification and *TP53* mutations in human cancer. *Nat Genet* **48**: 104–106. doi:10.1038/ng.3468

Wang L, Hu H, Pan Y, Wang R, Li Y, Shen L, Yu Y, Li H, Cai D, Sun Y, et al. 2014. *PIK3CA* mutations frequently coexist with *EGFR/KRAS* mutations in non-small cell lung cancer and suggest poor prognosis in *EGFR/KRAS* wildtype subgroup. *PLoS One* **9**: e88291. doi:10.1371/journal.pone.0088291

Williams RJ. 1992. Simple statistical gradient-following algorithms for connectionist reinforcement learning. *Mach Learn* **8**: 229–256. doi:10.1007/BF00992696

Yates LR, Campbell PJ. 2012. Evolution of the cancer genome. *Nat Rev Genet* **13**: 795–806. doi:10.1038/nrg3317

Yeang CH, McCormick F, Levine A. 2008. Combinatorial patterns of somatic gene mutations in cancer. *FASEB J* **22**: 2605–2622. doi:10.1096/fj.08-108985

Received January 6, 2023; accepted in revised form June 9, 2023.